*powders*

MDPI

*Article*

# Influence of Process Parameters on Porosity and Hot Cracking of AISI H13 Fabricated by Laser Powder Bed Fusion

**Siyuan Qin [1,*], Yutao Bo [1], Simone Herzog [1], Bengt Hallstedt [1], Anke Kaletsch [1,2] and Christoph Broeckmann [1,2]**

[1] Institute for Materials Applications in Mechanical Engineering, RWTH Aachen University, Augustinerbach 4, 52064 Aachen, Germany
[2] Institute of Applied Powder Metallurgy and Ceramics at RWTH Aachen University e.V. (IAPK), Augustinerbach 4, 52064 Aachen, Germany
* Correspondence: s.qin@iwm.rwth-aachen.de; Tel.: +49-(0)241-809-9547

**Abstract:** Laser powder bed fusion is an attractive manufacturing technology promising novel components for the aircraft, automobile, and medical industries. However, depending on the material, some defects in the parts, especially pores or microcracks, cannot be avoided in the LPBF process. To achieve a part with low defect density, the optimal parameter sets must be determined. Many investigations have focused on how laser speed and laser power influence the melting process and the relative density of as-built parts. In this study, we considered laser and heated powder beds as two energy input sources, represented by volume energy density and preheating temperature, respectively. The interaction of these two energy inputs for the fabrication of AISI H13 was investigated. It was found that high preheating temperatures shifted the optimal parameter sets from the low energy density area to the high energy density area. In addition, high preheating also led to hot cracking, which was confirmed with Scheil solidification simulations.

**Keywords:** laser powder bed fusion; preheating temperature; parameter optimization; porosity; hot cracking; AISI H13

check for updates

**Citation:** Qin, S.; Bo, Y.; Herzog, S.; Hallstedt, B.; Kaletsch, A.; Broeckmann, C. Influence of Process Parameters on Porosity and Hot Cracking of AISI H13 Fabricated by Laser Powder Bed Fusion. *Powders* **2022**, *1*, 184–193. https://doi.org/10.3390/powders1030012

Academic Editors: Eugene Olevsky and Elena Gordo

Received: 19 July 2022
Accepted: 7 September 2022
Published: 9 September 2022

**Publisher's Note:** MDPI stays neutral with regard to jurisdictional claims in published maps and institutional affiliations.

**Copyright:** © 2022 by the authors. Licensee MDPI, Basel, Switzerland. This article is an open access article distributed under the terms and conditions of the Creative Commons Attribution (CC BY) license (https://creativecommons.org/licenses/by/4.0/).

## 1. Introduction

Laser powder bed fusion (LPBF), also known as selective laser melting, is one of the additive manufacturing processes specified in ASTM F2792-12a. An outstanding feature of LPBF is its high manufacturing precision, making it suitable for complex structures in various industry applications [1], such as electric mobility [2,3], fuel cell [4], and aircraft applications [5]. However, this layer-by-layer process brings naturally process-related defects, such as pores and cracks, into the components, which are deleterious to the lifetime of the components [6,7].

Three types of porosity are observed in LPBF: gas porosity, keyhole porosity, and lack-of-fusion porosity [6]. To achieve high densities, process parameter optimization, in particular laser power (P) and laser speed (v), has been intensively investigated [6,8–14]. In these studies, the process window described in P vs. v maps are typically plotted. With high laser speed and low laser power, the low energy density area leads to insufficient melting and lack-of-fusion defects. In detail, lack-of-fusion appears if the overlap between melt pools is not sufficient to ensure the melting of all particles [15]. In contrast, the high energy density area causes balling and keyhole pores. Therefore, the medium energy area in the laser processing map is selected as the process window to produce parts with high relative density and without the above defects. Overall, a stable melting pool is critical to minimize defects, and highly dense components require relatively high energy input while avoiding keyholes [16]. As another high energy input source, a preheated powder bed can improve the printability of alloys [17–21]. However, only the optimal parameters

were considered within these studies. The interaction of preheating temperatures with laser parameters has rarely been illustrated.

Hot cracks are another type of defect that have been reported among different alloys, such as magnesium alloys [22], aluminum alloys [23,24], high-entropy alloys [25], and steels [26] produced by LPBF. Hot cracking during solidification results from the fracture of the semisolid films at the boundaries of dendrite grains [27]. The thin layers of the melting pool rapidly solidify during the LPBF process, which leads to dendritic microstructure mainly along the building direction. These long directional dendrite boundaries limit liquid feeding and act as very sharp notches which is conducive to solidification cracking [10]. Even though the hot crack susceptibility is determined by the chemical composition of alloys, the LPBF process parameters can also affect the formation of hot cracks [22]. For instance, the size of the melting pool is also relative to the formation of hot cracks [28].

The martensitic hot work tool steel AISI H13 has been widely investigated in the field of LPBF since it combines good printability with comparably high hardness [29]. The melt pool geometry of single tracks was categorized with various laser powers and laser speeds [9]. As for 3D parts, a relative density higher than 98% can be achieved with the optimal P and v sets [26,30–33]. Cracks were also observed in most of these studies [26,31–33]. Normally, stress-induced cracks can be avoided by heating the powder bed [32] and by reducing stresses from thermal gradients and martensite formation. However, hot cracks are mainly related to the solidification process [9] and might respond differently to powder bed heating.

In the presented work, instead of studying the effects of laser power and laser speed, we considered all laser parameters together as one energy input source, which is represented by the volume energy density. The interaction between the volume energy density and the preheating temperature as the second energy input source was investigated with a focus on porosity and hot crack density. In addition, the Scheil solidification simulation was applied to estimate the hot crack susceptibility. The obtained results broaden the knowledge about how preheated powder bed interacts with process parameters and influences porosity and hot crack density of H13 produced by LPBF.

## 2. Materials and Methods

Hot-work tool steel AISI H13 (DIN No. 1.2344, DIN X40CrMoV5-1) powder was atomized in argon atmosphere. The corresponding chemical composition of the powder according to the supplier (Steel Service Krefeld GmbH, Germany) is within the specification in DIN EN ISO 4957 [34], as shown in Table 1. The particle size distribution of AISI H13 powder was determined by laser diffraction (Partica LA-950, Horiba, The Netherlands). As presented in Figure 1, the powder particles are mainly spherical and distributed with $D_{10}$ = 28 µm, $D_{50}$ = 42 µm, and $D_{90}$ = 63 µm.

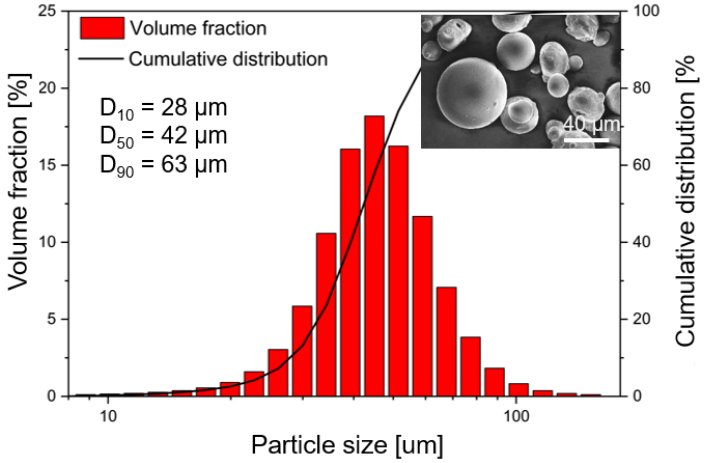


**Figure 1.** The particle size distribution and morphology of the H13 powder.

**Table 1.** Chemical composition of AISI H13 powder and standard range of chemical composition according to DIN EN ISO 4957 [34].

| | Chemical Composition [wt%] | | | | | | |
|---|---|---|---|---|---|---|---|
| | Fe | C | Cr | Mo | V | Si | Mn |
| LPBF powder | bal. | 0.4 | 5.4 | 1.29 | 1.14 | 0.91 | 0.32 |
| Standard | bal. | 0.35–0.42 | 4.8–5.5 | 1.2–1.5 | 0.85–1.15 | 0.8–1.2 | 0.25–0.5 |

The ReaLizer SLM 100 machine (ReaLizer GmbH Company, Germany), equipped with an Ytterbium fiber laser with a wavelength of 1070 nm and maximum output power of 200 W, was used for sample fabrication. Cubic samples of 10 × 10 × 10 $mm^3$ were fabricated under an argon atmosphere with an oxygen content below 300 ppm. An overpressure of about 30 mbar prevailed in the chamber in comparison to the ambient atmosphere. Samples were built without preheating or with 100 °C, 200 °C, or 400 °C preheating. The layer thickness of 50 µm was constant. Different process parameters were studied by varying laser power, laser speed (equals to d_point/t_expose), hatch distance, preheating temperature, and laser rotation angle, and 90 samples were built randomly positioned on the baseplate in seven building jobs.

The defect density was determined using image analysis. The cross sections parallel to the building direction were prepared by standard metallographic procedures including mounting, grinding, and polishing, and 16 optical images of each sample were taken with a magnification of 250 times to combine an overview of the cross section. Under this magnification, all defects can be clearly observed. These overviews were used for the density determination with the software ImageJ [35]. In this study, defects were separated into pores and hot cracks according to their circularity above or below 0.35, respectively. Cold cracks which typically appear at the surface of large components were not observed. Figure 2 presents an example of the defects in an optical overview separated into pores and hot cracks.

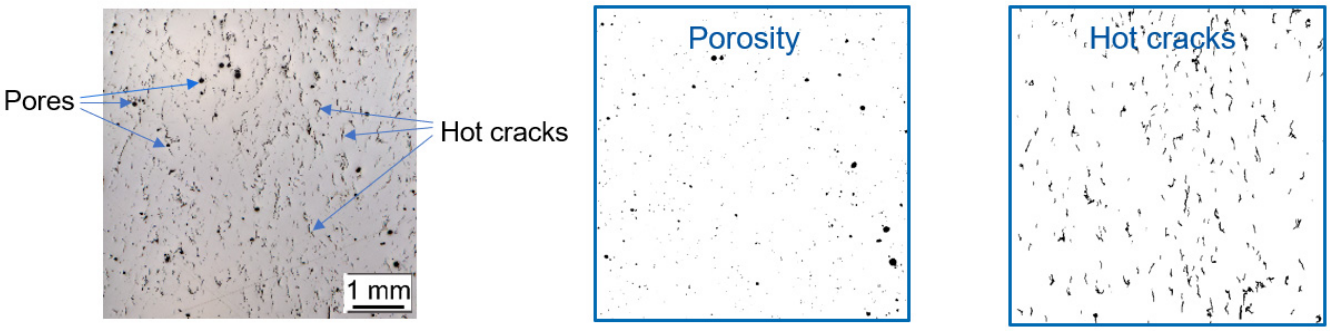


**Figure 2.** Defects in the cross section and corresponding separation into pores and hot cracks.

Samples were etched by Nital 5% at room temperature for 10 to 20 s to reveal the microstructure. Microstructure images were taken by an optical microscope and the scanning electron Helios Nanolab G3 CX (FEI, Hillsboro, OR, USA).

The Scheil solidification simulation with back diffusion was carried out in Thermo-Calc software (2021b, Thermo-Calc Software, Sweden) with the TCFE9 and MOBFE3 database for the AISI H13 powder chemical composition.

## 3. Results and Discussion

The LPBF process parameters in this study can be divided into three groups, volume energy density (VED), preheating temperature, and scan strategy, as illustrated in Figure 3. All of these parameters influence the relative density of as-built parts.

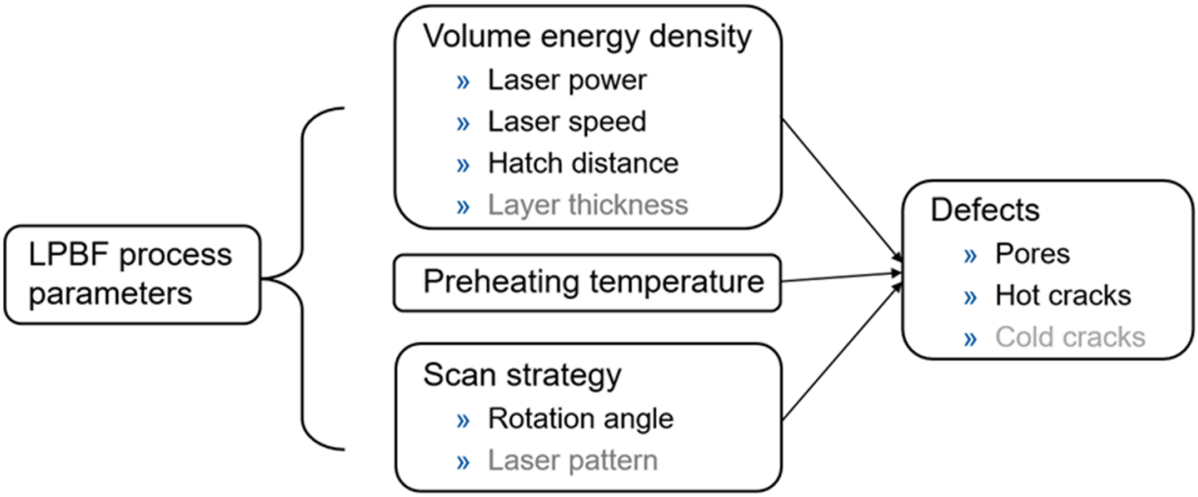


**Figure 3.** Category of LPBF parameters.

The volume energy density can be calculated by the equation:

$$VED = \frac{P}{v \cdot d \cdot t} \quad (1)$$

where $P$, $v$, $d$, and $t$ are laser power, laser speed, hatch distance, and layer thickness, respectively. VED describes the volumetric energy input from the laser and it is a sufficient parameter when we consider the part as a whole, for instance, the relative density analysis. However, the single-track melting behavior depends on the laser power and the laser speed, which determine the width and the depth of a melting pool [9].

The powder bed preheating system was developed for the LPBF process to avoid large thermal stresses in the material, especially for tool steels. Many investigations have confirmed that the preheating temperature influences microstructure and residual stresses of as-built parts [17,18,20,21,32]. In the present study, the heated powder bed is considered as another energy input source and, together with VED, determines the porosity and hot crack density.

The scanning strategy is the spatial moving route followed by the energy beam, which is of great importance to the local thermal profile and part quality. For a single layer, the scan strategy varies by different laser patterns, whereas, between two layers the scan strategy can be differentiated by laser rotation angle. Since the pores and hot cracks are mainly influenced by remelting process between the layers rather than the scan pattern in the single layer, only the rotation angle is discussed in the present study.

### *3.1. Influence of Process Parameters on Porosity*

As reviewed in the introduction, laser power–laser speed sets have been investigated comprehensively, from single-laser tracks to the whole as-built parts. Here, we move one step further, to illustrate how the two kinds of input energy source, namely the laser and the heated powder bed, influence the porosity. Figure 4 presents the effects of VED and preheating temperature on porosity. Without preheating or with 100 °C preheating, the lowest porosity is obtained in the VED range from 65 to 75 J/mm$^3$. For the higher preheating temperatures, 200 °C and 400 °C, samples built with the VED from 55 to 60 J/mm$^3$ show the lowest porosity. In other words, a high preheating temperature shifts the optimal parameter set to lower VEDs.

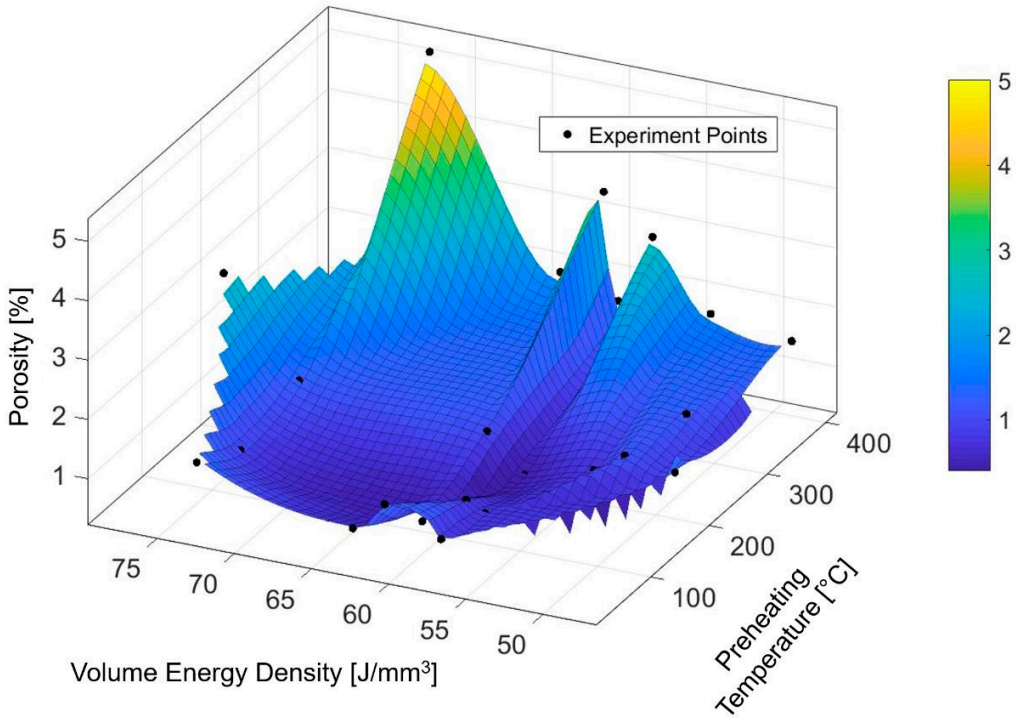


**Figure 4.** Porosity of samples versus volume energy density and preheating temperature.

To visualize the effects of the preheating temperature on porosity, exemplary cross sections of samples built with 73 J/mm$^3$ VED and various preheating temperatures are shown in Figure 5. With increasing temperature, more spherical pores are observed. In the overmelting area, it is common to observe spherical pores produced by entrapped gas or vapor [36]. This phenomenon indicates that the heated substrate, as another energy source to the powder, can effectively contribute energy by heat conduction to the laser melting process.

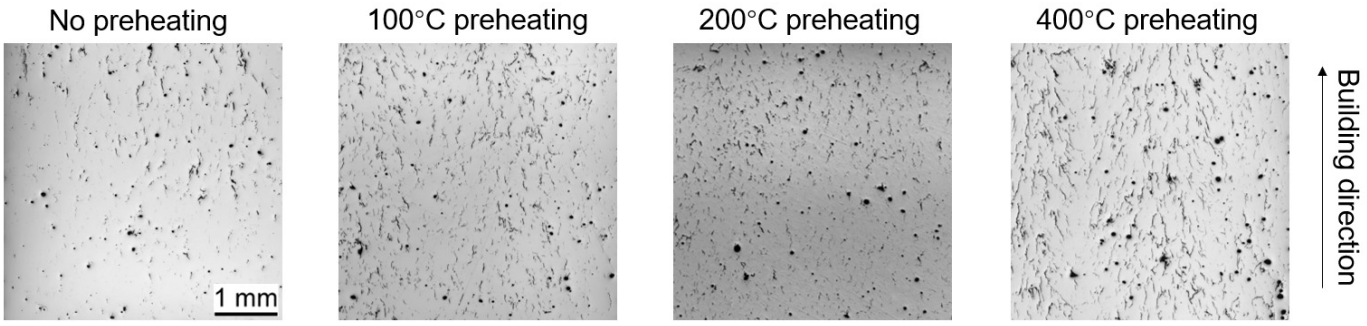


**Figure 5.** Cross-sections of samples with 73 J/mm$^3$ VED, 67° laser rotation angle and different preheating temperatures.

The laser scan rotation angle between the layers resulted in the rotation of heat flux and thus the alternation of the melting pool. Theoretically, a scan rotation of 67° leads to a more even temperature gradient and better fusion of the particles. Therefore, relatively homogeneous microstructure and mechanical properties have been reported with this kind of scan rotation [37–39]. As for porosity, a scan rotation of 67° can enhance densification during LPBF [38]. However, in our study, as shown in Figure 6, these two scan rotations result in similar average porosity values but with slightly less scatter with 67° laser rotation.

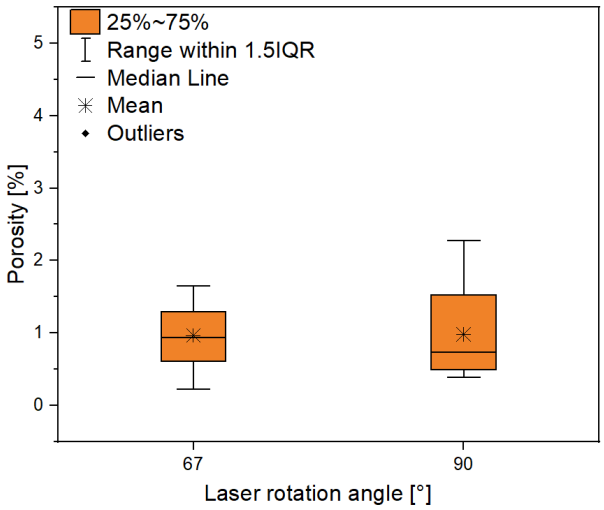


**Figure 6.** Statistical porosity analysis of samples built with 67° or 90° rotation angles. The compared samples are from the same batches and have the identical process parameters except rotation angle.

### *3.2. Influence of Process Parameters on Hot Crack Density*

Solidification and liquation cracking are well known from welding processes. Solidification (hot) cracks form in the melting pool and often reveal the dendritic morphology, whereas liquation cracks normally form in the heat-affected zone [40]. In the as-built parts, cracks can be detected from the cross-section, as shown in Figure 7. The melting tracks and dendritic solidification microstructure are revealed after etching. These cracks are located in the middle of the melting pool parallel to the building direction, which confirms their formation during solidification. Solidification cracking occurs at the final stage of solidification, where dendrites have grown almost fully into grains that are separated by a grain boundary liquid film, as illustrated in the back scattered electron (BSE) image.

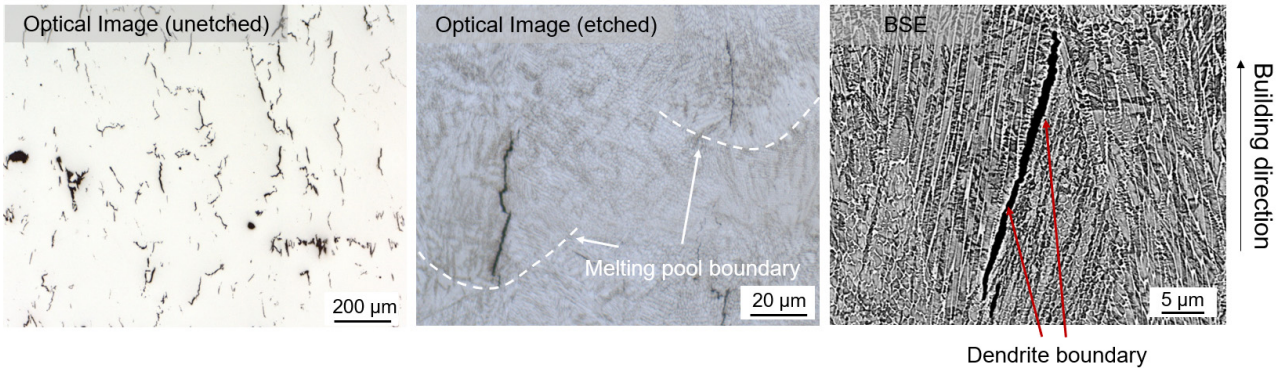


**Figure 7.** Hot cracks in optical image (with and without etching) and BSE image.

The crack density of samples with different VEDs and preheating temperatures are shown in Figure 8a. The hot crack density increased significantly at high preheating temperature, which is more precisely presented in Figure 8b. Up to 200 °C preheating, average hot crack densities are below 2%. This value surges to 3.8% at the 400 °C preheating, which indicates that when the preheating temperature is high enough to slow down the solidification, more hot cracks form in the melting pool.

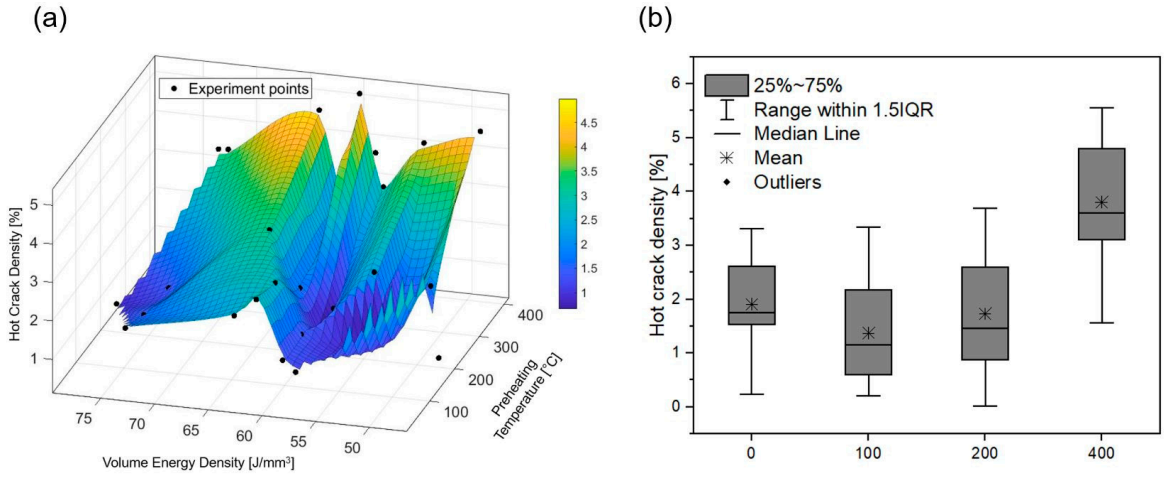


**Figure 8.** (**a**) Hot crack density of samples versus volume energy density and preheating temperature. (**b**) Statistical analysis of the hot crack density of samples built with different preheating temperatures.

The Scheil solidification simulation with back diffusion was performed to analyze how preheating temperatures influence the hot crack density. The index for the crack susceptibility during solidification was proposed by Kou [27], which is

$$\left|dT/d\left(f_s^{1/2}\right)\right| \quad near \quad f_s^{1/2} = 1, \tag{2}$$

where $T$ is the temperature and $f_s$ is the fraction of solid. This index reflects the length of the grain-boundary liquid channel between two neighboring grains, as illustrated in Figure 9a. The higher this index, the higher the susceptibility to hot cracking. Calculated curves of $T$ vs. $f_s^{1/2}$ for AISI H13 are shown in Figure 9b; $\left|\Delta T/\Delta\left(f_s^{1/2}\right)\right|$ was used as an approximation to compare the crack susceptibility. When the cooling rate increases from 1 K/s to 100 K/s, the temperate difference $\Delta T$ between ${f_s}^{1/2} = 0.98$ and ${f_s}^{1/2} = 0.99$ drops clearly (solid fraction $f_s = 0.96$ and $f_s = 0.98$, respectively), indicating lower susceptibility to hot cracking. As the cooling rate is higher than 100 K/s, hot crack susceptibility remains almost the same. This Scheil solidification simulation generally illustrates why more hot cracks formed at 400 °C preheating, whereas there is no significant difference with the preheating lower than 200 °C. However, we only assume that high preheating temperature leads to a lower cooling rate due to the smaller thermal gradient. Further sophisticated experiments and simulations are necessary to determine the cooling rate of the melting pool during the LPBF process.

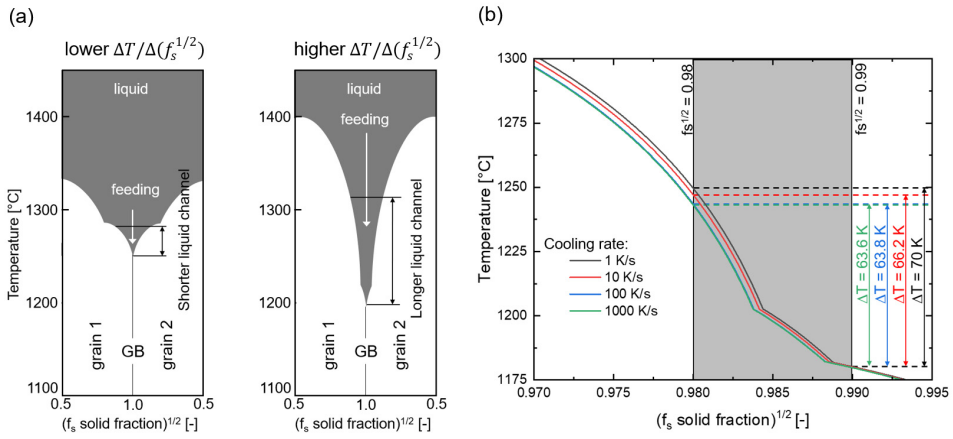


**Figure 9.** (**a**) Schematic illustration: effect of $\left|\Delta T/\Delta\left(f_s^{1/2}\right)\right|$ on liquid feeding at the grain boundary. (**b**) The comparison of crack susceptibility with different cooling rates by calculated $T$ vs. $f_s^{1/2}$ curves.

The statistical analysis of the hot crack density of parts built with 67° or 90° laser rotation angles is presented in Figure 10a, where samples built with the same process parameters but different laser rotation angles are compared. Considering all of the experimental data, there is no significant difference in hot crack density between the two rotation angles. However, for the optimized parameter sets with low porosity, the laser rotation angle of 67° leads to fewer hot cracks, which can be observed in the cross-sections in Figure 10b,c. With a scan rotation of 90°, hot cracks align with a distance corresponding to the hatch distance because the laser melted at the exact same position every two layers, and hot cracks always formed in the center of the melting pool. The scan rotation of 67° can avoid this repetition. Therefore, the parts built with the 67° scan rotation present fewer hot cracks.

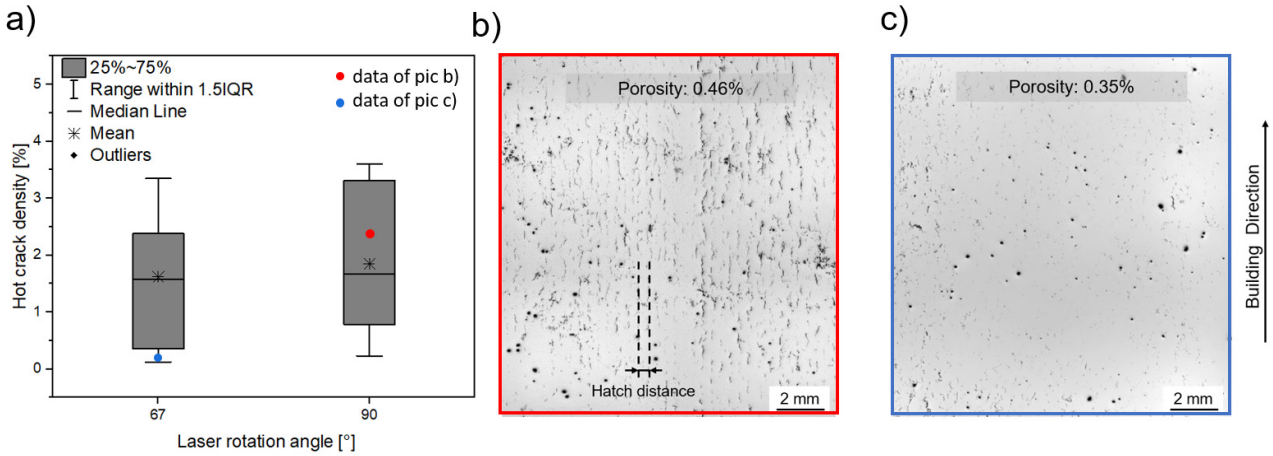


**Figure 10.** (**a**) Statistical analysis of the hot crack density of samples built with different laser rotation angles. The compared samples are from the same batches and have identical process parameters except rotation angle; (**b**,**c**) cross sections of samples b.

## 4. Conclusions

This study investigated the influence of volume energy density, preheating temperature, and scan rotation angle on porosity and hot cracking of as-built AISI H13 parts. The heated powder bed can help the laser to melt metallic particles. With increasing preheating temperature, the optimal parameter sets shift to low volume energy densities. For AISI H13, high preheating temperature results in more hot cracks, which can be explained by slower solidification. The scan rotation of 67° can to some extent alleviate hot cracking by avoiding the repeated solidification at same position. The Scheil solidification simulation with back diffusion can qualitatively predict the hot crack susceptibility. This can be particularly useful when comparing hot crack susceptibility for different alloy compositions. However, further investigations are necessary for more accurate calculations.

**Author Contributions:** Conceptualization, S.Q.; methodology, S.Q. and Y.B.; formal analysis, Y.B.; data curation, Y.B.; writing—original draft preparation, S.Q.; writing—review and editing, S.H., A.K. and B.H.; visualization, S.Q. and Y.B.; supervision, S.H., A.K., B.H. and C.B.; project administration, C.B.; funding acquisition, C.B. All authors have read and agreed to the published version of the manuscript.

**Funding:** The research was funded by the Deutsche Forschungsgemeinschaft (DFG, German Research Foundation) under Germany's Excellence Strategy—EXC-2023 Internet of Production—390621612.

**Data Availability Statement:** The data presented in this study are available on request from the corresponding author. The data are not publicly available because they are part of an ongoing study.

**Conflicts of Interest:** The authors declare no conflict of interest.

## References


1. Gu, D.; Shi, X.; Poprawe, R.; Bourell, D.L.; Setchi, R.; Zhu, J. Material-structure-performance integrated laser-metal additive manufacturing. *Science* **2021**, *372*, eabg1487. [CrossRef]
2. Stornelli, G.; Faba, A.; Di Schino, A.; Folgarait, P.; Ridolfi, M.R.; Cardelli, E.; Montanari, R. Properties of Additively Manufactured Electric Steel Powder Cores with Increased Si Content. *Materials* **2021**, *14*, 1489. [CrossRef] [PubMed]
3. Garibaldi, M.; Ashcroft, I.; Hillier, N.; Harmon, S.; Hague, R. Relationship between laser energy input, microstructures and magnetic properties of selective laser melted Fe-6.9%wt Si soft magnets. *Mater. Charact.* **2018**, *143*, 144–151. [CrossRef]
4. He, P.; Sun, C.; Wang, Y. Material distortion in laser-based additive manufacturing of fuel cell component: Three-dimensional numerical analysis. *Addit. Manuf.* **2021**, *46*, 102188. [CrossRef]
5. Gloria, A.; Montanari, R.; Richetta, M.; Varone, A. Alloys for Aeronautic Applications: State of the Art and Perspectives. *Metals* **2019**, *9*, 662. [CrossRef]
6. Gordon, J.V.; Narra, S.P.; Cunningham, R.W.; Liu, H.; Chen, H.; Suter, R.M.; Beuth, J.L.; Rollett, A.D. Defect structure process maps for laser powder bed fusion additive manufacturing. *Addit. Manuf.* **2020**, *36*, 101552. [CrossRef]
7. Kaletsch, A.; Qin, S.; Herzog, S.; Broeckmann, C. Influence of high initial porosity introduced by laser powder bed fusion on the fatigue strength of Inconel 718 after post-processing with hot isostatic pressing. *Addit. Manuf.* **2021**, *47*, 102331. [CrossRef]
8. Diaz Vallejo, N.; Lucas, C.; Ayers, N.; Graydon, K.; Hyer, H.; Sohn, Y. Process Optimization and Microstructure Analysis to Understand Laser Powder Bed Fusion of 316L Stainless Steel. *Metals* **2021**, *11*, 832. [CrossRef]
9. He, Y.; Zhong, M.; Beuth, J.; Webler, B. A study of microstructure and cracking behavior of H13 tool steel produced by laser powder bed fusion using single-tracks, multi-track pads, and 3D cubes. *J. Mater. Process. Technol.* **2020**, *286*, 116802. [CrossRef]
10. Stopyra, W.; Gruber, K.; Smolina, I.; Kurzynowski, T.; Kuźnicka, B. Laser powder bed fusion of AA7075 alloy: Influence of process parameters on porosity and hot cracking. *Addit. Manuf.* **2020**, *35*, 101270. [CrossRef]
11. Benn, F.; D'Elia, F.; van Gaalen, K.; Li, M.; Malinov, S.; Kopp, A. Printability, mechanical and degradation properties of Mg-(x)Zn elemental powder mixes processed by laser powder bed fusion. *Addit. Manuf. Lett.* **2022**, *2*, 100025. [CrossRef]
12. Cunningham, R.; Zhao, C.; Parab, N.; Kantzos, C.; Pauza, J.; Fezzaa, K.; Sun, T.; Rollett, A.D. Keyhole threshold and morphology in laser melting revealed by ultrahigh-speed x-ray imaging. *Science* **2019**, *363*, 849–852. [CrossRef]
13. Gong, H.; Rafi, K.; Gu, H.; Starr, T.; Stucker, B. Analysis of defect generation in Ti–6Al–4V parts made using powder bed fusion additive manufacturing processes. *Addit. Manuf.* **2014**, *1–4*, 87–98. [CrossRef]
14. Guzmán, J.; Nobre, R.d.M.; Nunes, E.R.; Bayerlein, D.L.; Falcão, R.B.; Sallica-Leva, E.; Neto, J.B.F.; Oliveira, H.R.; Chastinet, V.L.; Landgraf, F.J. Laser powder bed fusion parameters to produce high-density Ti–53%Nb alloy using irregularly shaped powder from hydride-dehydride (HDH) process. *J. Mater. Res. Technol.* **2021**, *10*, 1372–1381. [CrossRef]
15. Tang, M.; Pistorius, P.C.; Beuth, J.L. Prediction of lack-of-fusion porosity for powder bed fusion. *Addit. Manuf.* **2017**, *14*, 39–48. [CrossRef]
16. Khairallah, S.A.; Martin, A.A.; Lee, J.R.I.; Guss, G.; Calta, N.P.; Hammons, J.A.; Nielsen, M.H.; Chaput, K.; Schwalbach, E.; Shah, M.N.; et al. Controlling interdependent meso-nanosecond dynamics and defect generation in metal 3D printing. *Science* **2020**, *368*, 660–665. [CrossRef]
17. Qin, S.; Herzog, S.; Kaletsch, A.; Broeckmann, C. Effects of Pressure on Microstructure and Residual Stresses during Hot Isostatic Pressing Post Treatment of AISI M50 Produced by Laser Powder-Bed Fusion. *Metals* **2021**, *11*, 596. [CrossRef]
18. Mertens, R.; Vrancken, B.; Holmstock, N.; Kinds, Y.; Kruth, J.-P.; van Humbeeck, J. Influence of Powder Bed Preheating on Microstructure and Mechanical Properties of H13 Tool Steel SLM Parts. *Phys. Procedia* **2016**, *83*, 882–890. [CrossRef]
19. Ali, H.; Ma, L.; Ghadbeigi, H.; Mumtaz, K. In-situ residual stress reduction, martensitic decomposition and mechanical properties enhancement through high temperature powder bed pre-heating of Selective Laser Melted Ti6Al4V. *Mater. Sci. Eng. A* **2017**, *695*, 211–220. [CrossRef]
20. Riener, K.; Pfalz, T.; Funcke, F.; Leichtfried, G. Processability of high-strength aluminum 6182 series alloy via laser powder bed fusion (LPBF). *Int. J. Adv. Manuf. Technol.* **2022**, *119*, 4963–4977. [CrossRef]
21. Kunz, J.; Saewe, J.; Herzog, S.; Kaletsch, A.; Schleifenbaum, J.H.; Broeckmann, C. Influence of Powder Bed Temperature on Microstructure and Post Heat Treatment of High Speed Steel AISI M50 Processed by Laser Powder Bed Fusion. In Proceedings of the Euro PM2018 Proceedings 2018, Bilbao, Spain, 14–18 October 2018.
22. Liu, J.; Yin, B.; Sun, Z.; Wen, P.; Zheng, Y.; Tian, Y. Hot cracking in ZK60 magnesium alloy produced by laser powder bed fusion process. *Mater. Lett.* **2021**, *301*, 130283. [CrossRef]
23. Prasad, K.; Obana, M.; Ishii, Y.; Ito, A.; Torizuka, S. The effect of laser scanning strategies on the microstructure, texture and crystallography of grains exhibiting hot cracks in additively manufactured Hastelloy X. *Mech. Mater.* **2021**, *157*, 103816. [CrossRef]
24. Hyer, H.; Zhou, L.; Mehta, A.; Park, S.; Huynh, T.; Song, S.; Bai, Y.; Cho, K.; McWilliams, B.; Sohn, Y. Composition-dependent solidification cracking of aluminum-silicon alloys during laser powder bed fusion. *Acta Mater.* **2021**, *208*, 116698. [CrossRef]
25. Sun, Z.; Tan, X.P.; Descoins, M.; Mangelinck, D.; Tor, S.B.; Lim, C.S. Revealing hot tearing mechanism for an additively manufactured high-entropy alloy via selective laser melting. *Scr. Mater.* **2019**, *168*, 129–133. [CrossRef]
26. Wu, L.; Das, S.; Gridin, W.; Leuders, S.; Kahlert, M.; Vollmer, M.; Niendorf, T. Hot Work Tool Steel Processed by Laser Powder Bed Fusion: A Review on Most Relevant Influencing Factors. *Adv. Eng. Mater.* **2021**, *23*, 2100049. [CrossRef]
27. Kou, S. A criterion for cracking during solidification. *Acta Mater.* **2015**, *88*, 366–374. [CrossRef]

28. Kouraytem, N.; Chiang, P.-J.; Jiang, R.; Kantzos, C.; Pauza, J.; Cunningham, R.; Wu, Z.; Tang, G.; Parab, N.; Zhao, C.; et al. Solidification crack propagation and morphology dependence on processing parameters in AA6061 from ultra-high-speed x-ray visualization. *Addit. Manuf.* **2021**, *42*, 101959. [CrossRef]
29. Wang, J.; Liu, S.; Fang, Y.; He, Z. A short review on selective laser melting of H13 steel. *Int. J. Adv. Manuf. Technol.* **2020**, *108*, 2453–2466. [CrossRef]
30. Åsberg, M.; Fredriksson, G.; Hatami, S.; Fredriksson, W.; Krakhmalev, P. Influence of post treatment on microstructure, porosity and mechanical properties of additive manufactured H13 tool steel. *Mater. Sci. Eng. A* **2019**, *742*, 584–589. [CrossRef]
31. Fonseca, E.B.; Gabriel, A.H.; Araújo, L.C.; Santos, P.L.; Campo, K.N.; Lopes, E.S. Assessment of laser power and scan speed influence on microstructural features and consolidation of AISI H13 tool steel processed by additive manufacturing. *Addit. Manuf.* **2020**, *34*, 101250. [CrossRef]
32. Krell, J.; Röttger, A.; Geenen, K.; Theisen, W. General investigations on processing tool steel X40CrMoV5-1 with selective laser melting. *J. Mater. Process. Technol.* **2018**, *255*, 679–688. [CrossRef]
33. Kunz, J.; Herzog, S.; Kaletsch, A.; Broeckmann, C. Influence of initial defect density on mechanical properties of AISI H13 hot-work tool steel produced by laser powder bed fusion and hot isostatic pressing. *Powder Metall.* **2021**, *8*, 1–12. [CrossRef]
34. *ISO 4957:2018*; Tool Steels. ISO: Geneva, Switzerland, 2018.
35. Schindelin, J.; Arganda-Carreras, I.; Frise, E.; Kaynig, V.; Longair, M.; Pietzsch, T.; Preibisch, S.; Rueden, C.; Saalfeld, S.; Schmid, B.; et al. Fiji: An open-source platform for biological-image analysis. *Nat. Methods* **2012**, *9*, 676–682. [CrossRef] [PubMed]
36. Martin, A.A.; Calta, N.P.; Khairallah, S.A.; Wang, J.; Depond, P.J.; Fong, A.Y.; Thampy, V.; Guss, G.M.; Kiss, A.M.; Stone, K.H.; et al. Dynamics of pore formation during laser powder bed fusion additive manufacturing. *Nat. Commun.* **2019**, *10*, 1987. [CrossRef]
37. Guan, K.; Wang, Z.; Gao, M.; Li, X.; Zeng, X. Effects of processing parameters on tensile properties of selective laser melted 304 stainless steel. *Mater. Des.* **2013**, *50*, 581–586. [CrossRef]
38. Qin, H.; Fallah, V.; Dong, Q.; Brochu, M.; Daymond, M.R.; Gallerneault, M. Solidification pattern, microstructure and texture development in Laser Powder Bed Fusion (LPBF) of Al10SiMg alloy. *Mater. Charact.* **2018**, *145*, 29–38. [CrossRef]
39. Arısoy, Y.M.; Criales, L.E.; Özel, T.; Lane, B.; Moylan, S.; Donmez, A. Influence of scan strategy and process parameters on microstructure and its optimization in additively manufactured nickel alloy 625 via laser powder bed fusion. *Int. J. Adv. Manuf. Technol.* **2017**, *90*, 1393–1417. [CrossRef]
40. Kou, S. Solidification and liquation cracking issues in welding. *JOM* **2003**, *55*, 37–42. [CrossRef]